ACS OMEGA

Open Access

http://pubs.acs.org/journal/acsodf

Article

CuO/TiO_2/ZnO NPs Anchored Hydrogen Exfoliated Graphene: To Comprehend the Role of Graphene in Catalytic Reduction of p-Nitrophenol

Meerambika Behera,[⊥] Fatimah Othman Alqahtani,* Sankha Chakrabortty,[⊥] Jayato Nayak, Shirsendu Banerjee, Ramesh Kumar, Byong-Hun Jeon,* and Suraj K Tripathy*

Cite This: *ACS Omega* 2023, 8, 42164−42176

Read Online

ACCESS | Metrics & More | Article Recommendations | Supporting Information

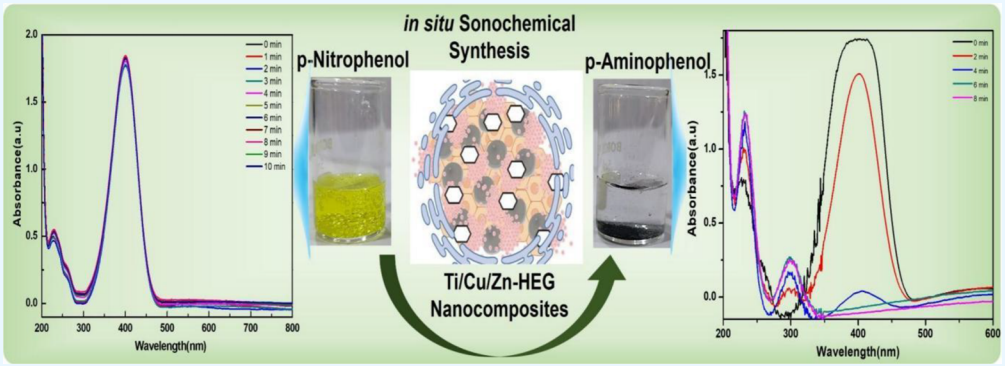

ABSTRACT: The present study deals with sonochemically in situ synthesis of a novel functional catalyst using hydrogen exfoliated graphene (HEG) supported titanium dioxide (TiO_2) and copper sulfate ($CuSO_4$) doped with zinc oxide (ZnO) (abbreviated as Ti/Cu/Zn-HEG). The synthesis of the Ti/Cu/Zn-HEG nanocomposite (NCs) catalyst was confirmed through its characterizations by XRD, SEM-EDX, TEM, XPS, FTIR, and BET methods. It was assessed for catalytic conversion of a model aromatic compound *para*-nitrophenol (p-NP) in an aqueous solution. The p-NP is a nitroaromatic compound that has a toxic and mutagenic effect. Its removal from the water system is necessary to protect the environment and living being. The newly synthesized Ti/Cu/Zn-HEG NCs were applied for their higher stability and catalytic activity as a potential candidate for reducing p-NP in practice. The operating parameters, such as p-NP concentration, catalyst dosage, and operating time were optimized for 150 ppm, 400 ppm, and 10 min through response surface methodology (RSM) in Design-Expert software to obtain the maximum reduction p-NP up to 98.4% at its normal pH of 7.1 against the controls (using HEG, Ti/Cu-HEG, and Zn-HEG). Analysis of variance of the response suggested the regression equation to be significant for the process with a major impact on catalyst concentration and operating time. The model prediction data (from RSM) and experimental data were corroborated well as reflected through model's low relative error (RE < 0.10), high regression coefficient (R^2 > 0.97), and Willmott *d*-index ($d_{will\text{-}index}$ > 0.95) values.

1. INTRODUCTION

Heterogeneouslycatalyzed reactions are crucial for producing commodities and consumer products, such as chemicals, pharmaceuticals, and polymers, accounting for approximately 25% of industrial energy usage.[1,2] In the future, most energy-intensive chemical industries will essentially count on heterogeneous catalysis to secure carbon-neutral operations and sustainable manufacturing.[3] Therefore, an increasing demand is for the development of more efficient and environmentally friendly industrial catalysts. It is possible, in theory, to design atomically precise materials with self-regenerating sites of activity for use as catalysts in selective chemical/biochemical reactions.[4] Noble metallic nanoparticles (NPs) have a large surface area, many functioning surface areas, and the potential for quantum confinement effects, making them a few of the most extensively studied heterogeneous catalysts.[5] In particular, the effectiveness of these new catalysts for the hydrogenation reaction is measured by how well they reduce p-nitrophenol (p-NP) by using $NaBH_4$ as a model reaction.[6]

Nitrophenols or nitroaromatic compounds are widely discharged in water bodies due to their overuse in

Received: June 1, 2023
Revised: September 15, 2023
Accepted: September 27, 2023
Published: November 1, 2023

manufacturing pharmaceuticals, petrochemicals, paints, plastic, pesticides, and dye.[7,8] Considering the severe environmental effect on soil, groundwater, and air, US Environmental Protection Agency has listed p-NP as one of the priority pollutants and recommended its concentration <10 ppb in surface water.[9] Highly stable and soluble p-NP compounds show recalcitrance in natural systems and largely resistance toward bioremediation.[10] Other methods, such as solvent extraction, adsorption, and advanced oxidation processes, either transfer pollutants from one phase to another or produce secondary pollutants. The catalytic transformation of p-NP to industrially useful *p*-aminophenol (p-AP) molecules has received specific attention owing to its unique potential to treat environmentally hazardous chemicals in a greener and more economical approach focusing on the circular economy.[11]

There is a lot of focus on industries to find alternatives to the metal NPs traditionally used for catalytic conversion of p-NP to p-AP.[12−14] It has been proposed that nanocomposites (NCs) made from supported carbon materials, viz., graphene and silica, were used to accommodate nanocatalyst to enhance their stability and durability.[15] These NCs are made by meticulously designing their chemical makeups and/or morphologies. Maghemite/zinc oxide nanocomposites were used for the catalytic reduction of p-NP, as reported by Behera et al.[16] Thus, exploration of non-noble-metal-based catalysts, high efficiency, and requirement of low catalyst loading, such as metal oxide/graphene-based NCs, have recently been proposed as potential candidates to overcome the scale-up limitations. Graphene is expected to provide a large and active surface area, higher chemical stability, and higher electrical conductivity for the anchoring of metal oxides. It can also help in the adsorption of p-NP, thus, enhancing its proximity toward the catalyst, which promotes the catalytic process. Jacob et al. used $NiCo_2O_4$ NPs anchored on reduced graphene oxide for catalytic reduction of p-NP.[17] Guo et al. reported the plasma-catalytic degradation of aqueous p-NP with graphene-ZnO.[18] However, experiments with these catalysts lack reusability, optimization of process parameters, and economic analysis, which limits their large-scale trials. Nevertheless, efficient p-NP reduction through the mutual interaction of different parametric factors, such as p-NP concentration, catalytic dosage, and operating time, can be planned using a tool (central composite design) from the response surface methodology of Design-Expert software. Optimization of the process parameters for obtaining the most favorable conditions for the catalytic process is useful to bring maximum catalytic activity with minimum time and chemical usage by checking the cross-effects of the different parameters at a time.[19,20]

Graphene NCs have significant prospects for various applications, including energy storage and energy conversion devices, because of their improved electrical and electronic properties and the synergistic interaction between graphene and inorganic NPs.[21,22] Consequently, due to their unique ability to combine desirable qualities of building blocks for a specific purpose, interest in graphene-based materials has been steadily increasing.[25,26] Highly porous graphene is expected to accommodate more catalytic metal oxides, including active hydrogen molecules, for better p-NP reduction. Furthermore, graphene has shown exceptional electronic conductivity due to special sp^2 hybridization of carbon bonds for better delocalization of electrons.[27] Its electronic conductivity can be improved by adding various inorganic metals as nanocatalysts.[23,24] Different metal and metal oxide NPs have been encased on graphene to prevent the accumulation of individual graphene sheets, which is brought on by strong van der Waals interactions between graphene layers.[28] In the present study, a novel functional NCs catalyst (Ti/Cu/Zn-HEG) was synthesized using nanocatalysts (TiO_2/CuO/ZnO) impregnated in hydrogen-exfoliated graphene (HEG) via coprecipitation method for p-NP reduction under response surface-optimized experimental conditions. It is hypothesized that the presence of different metal oxides impregnated on graphene sheet may facilitate the delocalization of electrons, which in turn may augment the overall reduction efficacy and catalytic life span of the NC system. In the course of further discussion, the results endorsed the proposed hypothesis. Theory and experimental results supported Ti/Cu/Zn-HEG as a suitable catalyst for p-NP reduction under the model experimental conditions.

2. EXPERIMENTAL SECTION

2.1. Materials and Methods. All the chemicals and reagents used in the reaction process are of analytical reagent grade except titanium dioxide (TiO_2), a photocatalytic grade product of SRL, India. Graphite flakes, *N*-methyl-pyrrolidone, sulfuric acid (H_2SO_4), potassium permanganate ($KMnO_4$), copper oxide (CuO), sodium nitrate ($NaNO_3$), and sodium borohydride ($NaBH_4$) were purchased from Sigma-Aldrich, USA. p-NP ($C_6H_5NO_3$) and sodium hydroxide (NaOH) were procured from SRL, India. Zinc nitrate hexahydrate ($ZnNO_3 \cdot 6H_2O$) is a product of HIMEDIA, India. Absolute ethanol was utilized as the solvent for the sol−gel process. The experiment used all of the chemicals and reagents received in their original state.

2.2. Synthesis of Ti/Cu-HEG NCs. Improved Hummer's method[23,29,30] synthesized graphite oxide (GO) by chemical oxidation and exfoliation of graphite flakes followed by hydrogen gas expulsion for 2 min at 180 °C to achieve GO's extended surface area named HEG. The Ti-HEG was synthesized using a conventional ultrasonic-assisted sol−gel process by mixing 2 g of TiO_2 in 30 mL of absolute ethanol and sonicated for about 30 min. A carbon binder, glucose (0.01M) solution, and 3 g of CuO solution were prepared and added slowly into the Ti-HEG mixture.[31,32,37] The mixture was sonicated for another 2 h, allowing the solid residues to settle properly. The precipitate was collected, dried, and calcined for 2 h at 500 °C and labeled Ti/Cu-HEG.

2.3. Synthesis of Ti/Cu/Zn-HEG Nanocomposites. A solution of 50 mg of Ti/Cu-HEG in 100 mL of distilled water (DW) was sonicated and kept on a hot plate at 500 rpm and 80 °C. The ZnO solution was prepared (by dissolving 30 mg of 10 mM zinc nitrate hexahydrate in 10 mL of DW and 2 M NaOH). A 3.5 mL aliquot of freshly prepared ZnO solution was mixed into the Ti/Cu/Zn-HEG and adjusted to a total volume of 10 mL. The resulting slurry was continuously stirred for 2 h until its settlement at the bottom. The filtered catalyst was dried in the oven and muffle-fired for an hour at 500 °C to obtain Ti/Cu/Zn-HEG catalyst.[20,33]

2.4. Characterization Techniques. X-ray diffraction was used to study the NC phases and crystal structures (Xpert Pro, PAN Analytical, UK). PerkinElmer Spectrum IR Version 10.7.2 assessed the surface activity and organic contaminants. NC morphology was examined using scanning electron microscopy (ZEISS Supra-40) and high-resolution transmission electron microscopy (JEOL JEM 2100 PLUS). SEM-EDS identified NC system elements. The Quanatchrome

https://doi.org/10.1021/acsomega.3c03859
ACS Omega 2023, 8, 42164−42176

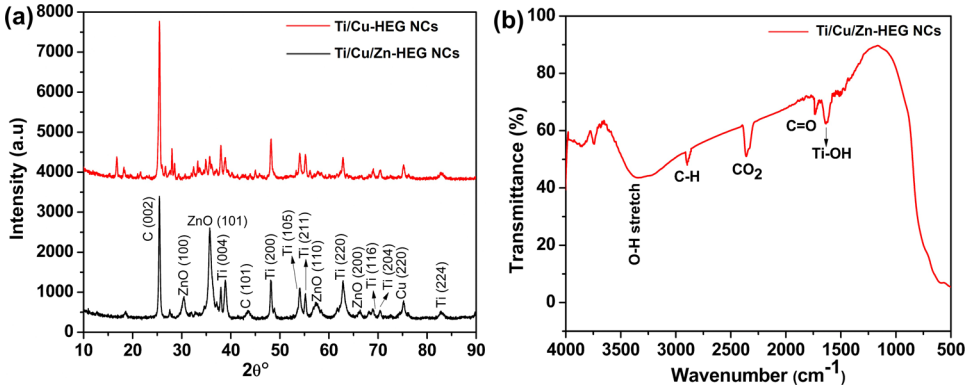

Figure 1. (a) XRD pattern of Ti/Cu-HEG NCs and Ti/Cu/Zn-HEG NCs and (b) FTIR spectra of Ti/Cu/Zn-HEG NCs.

Novae 2200 system measured the pore size distribution and surface area using BET and BJH methods. X-ray photoelectron spectroscopy experiments were performed with Thermo Fisher Scientific's ESCALAB Xi+ and an Al K X-ray source.

2.5. Catalytic Experiments. To transform into p-nitrophenol (p-NP) in the presence of $NaBH_4$, the Ti/Cu/Zn-HEG NCs were tracked in a UV/vis spectrophotometer (Agilent, Carry 100) to determine their catalytic interest. In summary, a 1 mL quartz cuvette with a temperature of over 80% was loaded with 0.2 mM p-NP and 15 mM freshly prepared $NaBH_4$ aqueous solution. The solution's color shifted to yellow almost instantly. UV/vis spectra of the solution were recorded regularly, with a scanning range of 200−800 nm. The reaction, detected through a color change, took 10 min to complete. Several control experiments were conducted using various catalysts, including hydrogen exfoliated graphene coupled with zinc oxide (HZ), hydrogen exfoliated graphene coupled with zinc oxide/titanium dioxide (HTC), and only zinc oxide. The purpose of these control reactions was to gain a better understanding of the influence of $NaBH_4$ on the catalytic reaction. By comparing the results obtained from these different setups, researchers aimed to elucidate the specific role of $NaBH_4$ in the catalytic process and its interaction with the catalysts, shedding light on the underlying mechanisms at play. The formula can determine the catalytic conversion efficiency of p-NP during the reaction process.[34]

$$\text{Conversion efficiency of p-NP} = \frac{C_0 - C_t}{C_0} \times 100\% \quad (1)$$

where C_0 is the initial concentration of p-NP (ppm) measured at time, $t = 0$, and C_t is the final concentration of p-AP (ppm) measured at time t.

2.6. Optimization of Process Parameters. Multiple experiments were run to fine-tune various parameters to move forward with finer elaboration. Experiments with varying concentrations of p-NPs, catalyst doses, pH values, and other factors were conducted in naturally occurring air. Ti/Cu-HEG: ZnO concentrations were 50, 100, 150, and 200 ppm, and the ratio of Ti/Cu-HEG: ZnO was 1:0.25, 1:0.5, 1:1, and 1:1.5. The pH of the solution was measured at 3, 5, 7, 9, and 11 using a pH ion meter, and the amount of catalyst used ranged from 200 to 800 (ppm).

2.7. Order of Reaction and Rate Constant. Analysis of reaction data can be done by the differential method to calculate reaction order.[20]

For any reaction A → products with unknown order n, the rate expression may be written as

$$-\frac{dC_A}{dt} = kC_A^{\,n} \quad (2)$$

where $-dC_A/dt$ is the rate of disappearance of A (the negative sign indicates that the concentration of the reactant is decreasing) and k is the rate constant with units $(\text{time})^{-1}$ $(\text{concentration})^{1-n}$.

Solving eq 2 by taking logarithms in both LHS and RHS, we obtain

$$\ln\left(-\frac{dC_A}{dt}\right) = \ln k + n \ln C_A \quad (3)$$

Equation 3 represents a straight line with ln k as the intercept and n as the slope. The slopes of the tangents drawn (a minimum of three tangents are required) on the concentration vs time plot can give the values of $-dC_A/dt$. Finally, $\ln(-dC_A/dt)$ vs the logarithms of corresponding concentrations ($\ln C_A$) can be plotted, and the slope obtained gives us the reaction order.[35,36] The average value of k can now be obtained from eq 2.

2.8. Process Optimization through Response Surface Methodology (RSM). Maximum conversion of p-NP into p-AP was determined through an array of experiments designed to optimize the system parameters. The response (the efficiency of the conversion) was the only dependent variable in a set of 20 experiments that manipulated three independent variables. Within a time frame of 10 min, the most effective conversion parameters are as follows: p-NP concentrations of 50, 100, 150, and 200 ppm; catalyst Ti/Cu/Zn-HEG NCs concentrations of 200, 400, 600, and 800 ppm; and pH values of 3, 5, 7, 9, and 11.

2.9. Reusability Potential of Ti/Cu/Zn-HEG NCs. After completion of the reaction, 2 mL of samples was collected in centrifuge tubes. The Ti/Cu/Zn-HEG NCs were retrieved after being washed (thrice) with DW and centrifuged for 10 min at 5000 rpm. The NCs were dried in a hot-air oven at 60 °C for 8 h before being employed in subsequent catalysis.[37]

3. RESULTS AND DISCUSSION

3.1. Characterizations. XRD is commonly used to analyze the underlying crystalline phases in materials both qualitatively and quantitatively. XRD patterns of Ti/Cu-HEG and Ti/Cu/Zn-HEG NCs are displayed in Figure 1a. The peaks at 2θ = 25.4° and 43.5° correspond to hkl values (002) and (101) of graphitic planes, respectively. However, the XRD profile of Ti/Cu/Zn-HEG NCs indicates a prominent broad peak at a 2θ value of around 25, which can be attributed to the exfoliated

https://doi.org/10.1021/acsomega.3c03859
ACS Omega 2023, 8, 42164−42176

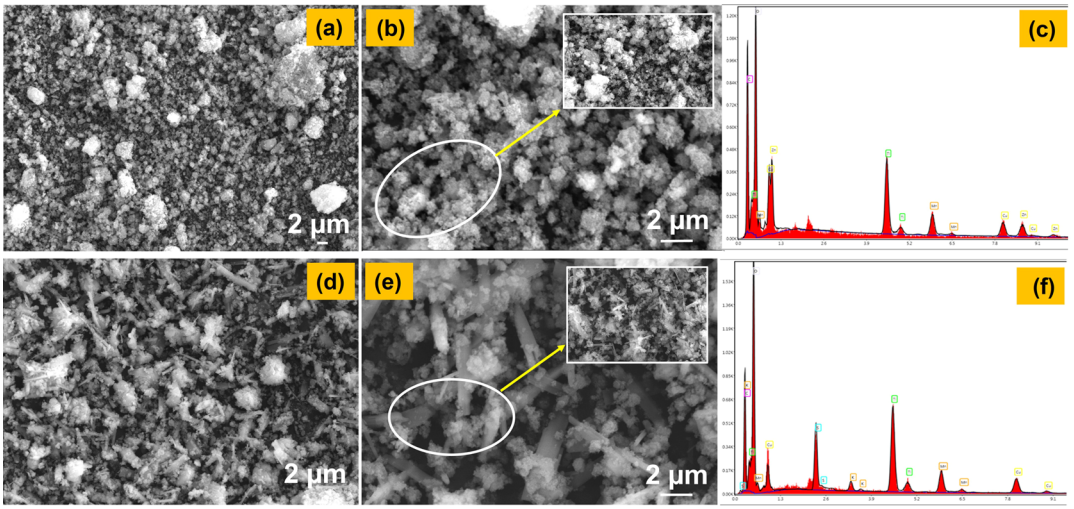

Figure 2. SEM images of (a,b) represent Ti/Cu/Zn-HEG NCs and (d,e) Ti/Cu-HEG NPs; (c,f) show the SEM-EDS spectra of respective materials.

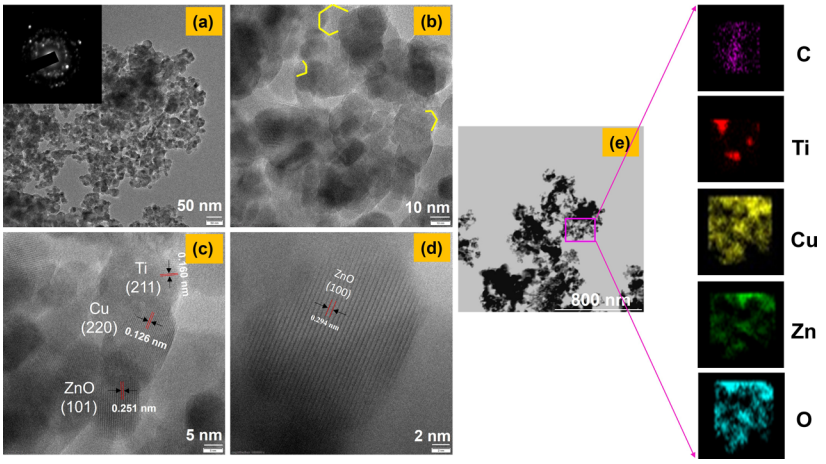

Figure 3. TEM images of (a,b) Ti/Cu/Zn-HEG NCs at different resolutions (inset: SAED pattern), (c,d) *d*-spacing, and (e) HAADF pattern.

graphene concentration levels. The graphite phase in the stacked layers of exfoliated graphene is represented by the peak reflection in the (002) plane (JCPDS 41-1487). The peak development at 43.5° can be explained by the covalently linked hydrogen atoms on the exfoliated graphene's surface.[38,39] Moreover, the peaks pointed at 37.9° (004), 48.3° (200), 54.1° (105), 55.2° (211), 62.7° (220), 68.4° (116), 69.9° (204), and 82.8° (224) can be referred to the TiO_2 anatase phase and its crystallinity form. JCPDS file no. 211272 is in good accord with these values.[40−42] Further, the diffraction peak at 2θ value 75.2° having the corresponding plane (220) confirms the presence of copper in Ti/Cu/Zn-HEG NCs.[43,44] The 2θ peaks at 31.4° (100), 36.1° (101), 57.5° (110), and 66.3° (200) can be referenced to the hexagonal wurtzite structure of ZnO. According to JCPDS card number 01-007-2551, the above planes relate to the crystal planes and hexagonal crystal geometry.[45,46] No peak correlates with any alloys or other structural formations. Using Scherrer's equation, the mean crystallite diameter (MCD) of Ti/Cu/Zn-HEG NCs was determined to be around 25−30 nm.

FTIR helps to ascertain the level of surface activity and the organic contaminants on the catalyst's surface. The FTIR spectra of the newly synthesized Ti/Cu/Zn-HEG NCs are displayed in Figure 1b. It is observed that the −OH functional group is responsible for a broad band around 3320 cm^{-1} in the Ti/Cu/Zn-HEG NCs. In addition, the OH stretching frequency is accountable for water molecule absorption on the surface of the NCs. Further, a small sharp peak at 2892.4 cm^{-1} is attributed to the −C−H stretching of alkanes and the alkyl functional group. The exfoliated graphene sheets in the medium benefit from these functional groups. The peak at 2355 cm^{-1} is assigned to ambient CO_2 adsorbed on nanocomposites' surfaces. A small sharp peak at 1728.6 cm^{-1} might correspond to the −C═O stretching of the carbonyl group, and an absorption band at 1634 cm^{-1} is depicted as the Ti−OH bending in the Ti/Cu/Zn-HEG catalyst. Each functional group is critical in sustaining the efficiency level of Ti/Cu/Zn-HEG NCs for catalytic conversion.[46,47]

The surface structure of the materials can have a significant impact on the catalysis of the reaction, which is reflected by SEM-EDS images for Ti/Cu/Zn-HEG and Ti/Cu-HEG NCs in Figure 2. In Ti/Cu/Zn-HEG NCs (Figure 2a,b), near-spherical and porous structures were observed in a vaguely agglomerated form. These structures can be predicted as the deposition of zinc oxide nanoparticles. A slightly uneven and disorganized structure on a wide scale with elongated sheetlike structures is shown in Ti/Cu-HEG NCs (Figure 2d,e). Agglomerates form on the synthesized materials, and TEM

https://doi.org/10.1021/acsomega.3c03859
ACS Omega 2023, 8, 42164−42176

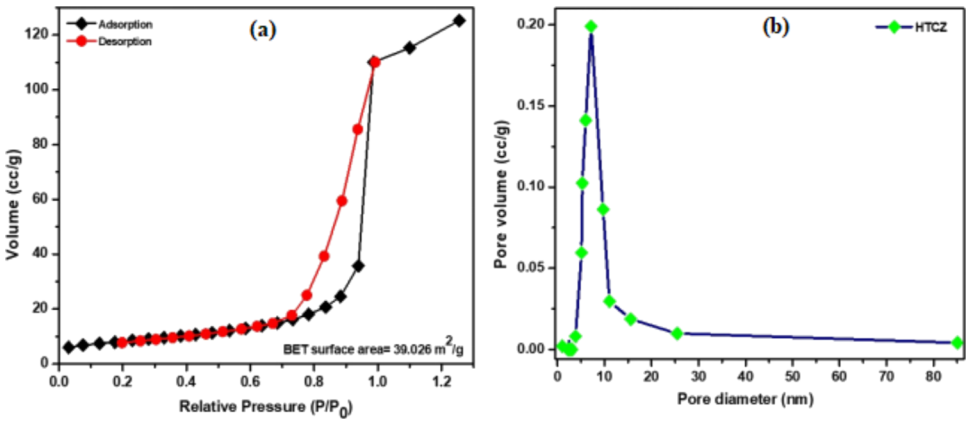

Figure 4. (a) displays the N_2 adsorption−desorption (BET) isotherm of Ti/Cu/Zn-HEG NCs and (b) represents its BJH pore size distribution curve.

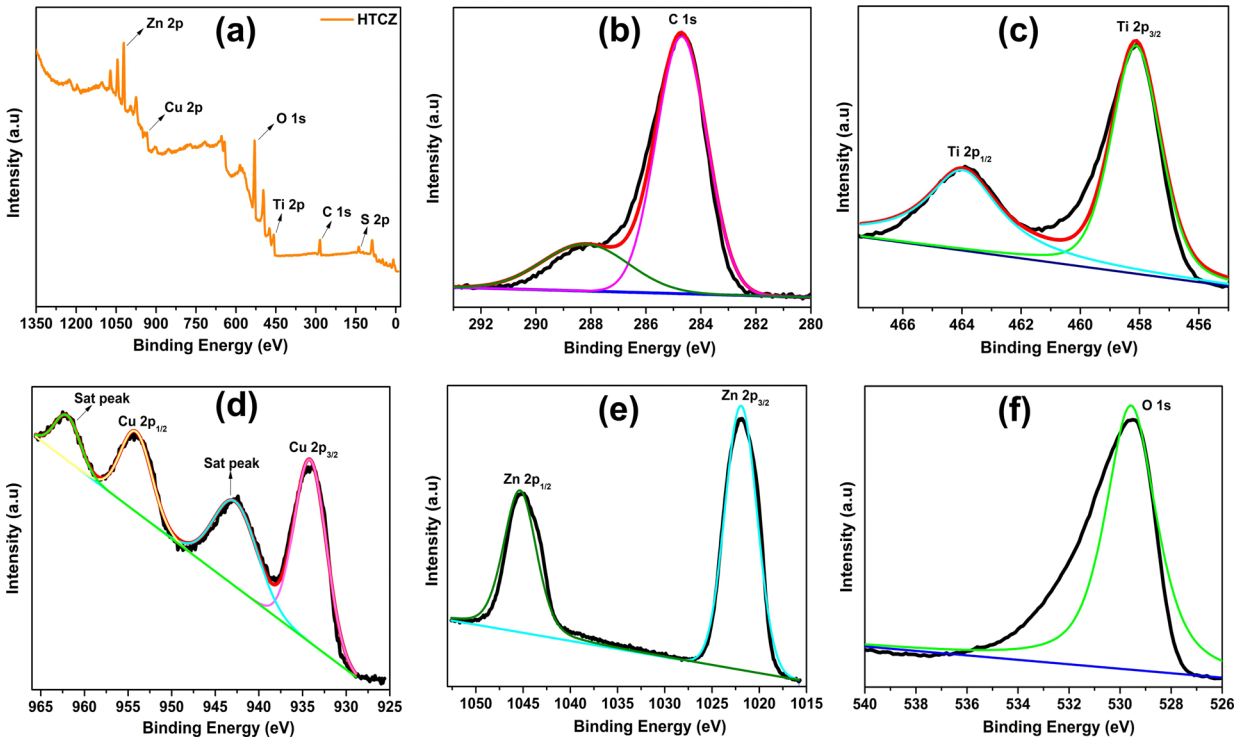

Figure 5. Representative XPS spectra of Ti/Cu/Zn-HEG NCs: (a) all elements, (b) carbon, (c) titanium, (d) copper, (e) zinc, and (f) oxygen, respectively, present in Ti/Cu/Zn-HEG NCs.

examinations are conducted to obtain improved surface morphology data.[48−50] Further, EDS images in Figure 2c,f confirm the elements in the synthesized Ti/Cu/Zn-HEG NCs. Compared to EDS data of Ti/Cu-HEG NCs, the Zn and O peaks of ZnO NPs are fairly evident in the EDS spectra of Ti/Cu/Zn-HEG NCs. In the case of Ti/Cu/Zn-HEG NCs, the weight percentages of C, O, Ti, Cu, and Zn were found to be at 31.42, 40.57, 10.36, 6.35, and 6.54%, respectively, while in Ti/Cu-HEG NCs, the weight percentages of C, O, Ti, and Cu were at 25.1, 44.89, 12.63, and 6.95%.

Ti/Cu/Zn-HEG NCs were subjected to TEM investigation to understand better their morphological patterns and crystal properties, which are displayed in Figure 3. At various magnifications, Figure 3a,b depicts different significant patterns and even more realistic data regarding the revealed crystal faces of Ti/Cu/Zn-HEG NCs which seemed to be in 20−30 nm size. Furthermore, the inset image in Figure 3a depicts the selected area electron diffraction (SAED) pattern of Ti/Cu/Zn-HEG NCs, which offers information about the crystallinity of the generated NCs. The coordinated rings of bright spots are observed in the SAED patterns. These motifs reflect the polycrystalline property. The crystallographic planes of the unit cells that make up the specimen diffract the electron beam. The *d*-spacing and lattice fringes of each element in the crystalline unit of Ti/Cu/Zn-HEG NCs can be seen in Figure 3c,d. The cross-linked fringes and asymmetrical patterns of the synthesized NCs help the nanocomposite to achieve high-quality results and contribute to the rigidity of the structure. Based on its atomic number (αZ^2), the mass-to-thickness idea of the elements present is outlined in Figure 3e by scanning TEM (S-TEM) with a high-angle annular dark field (HAADF).[51−54] Each element's atomic number determines

https://doi.org/10.1021/acsomega.3c03859
ACS Omega 2023, 8, 42164−42176

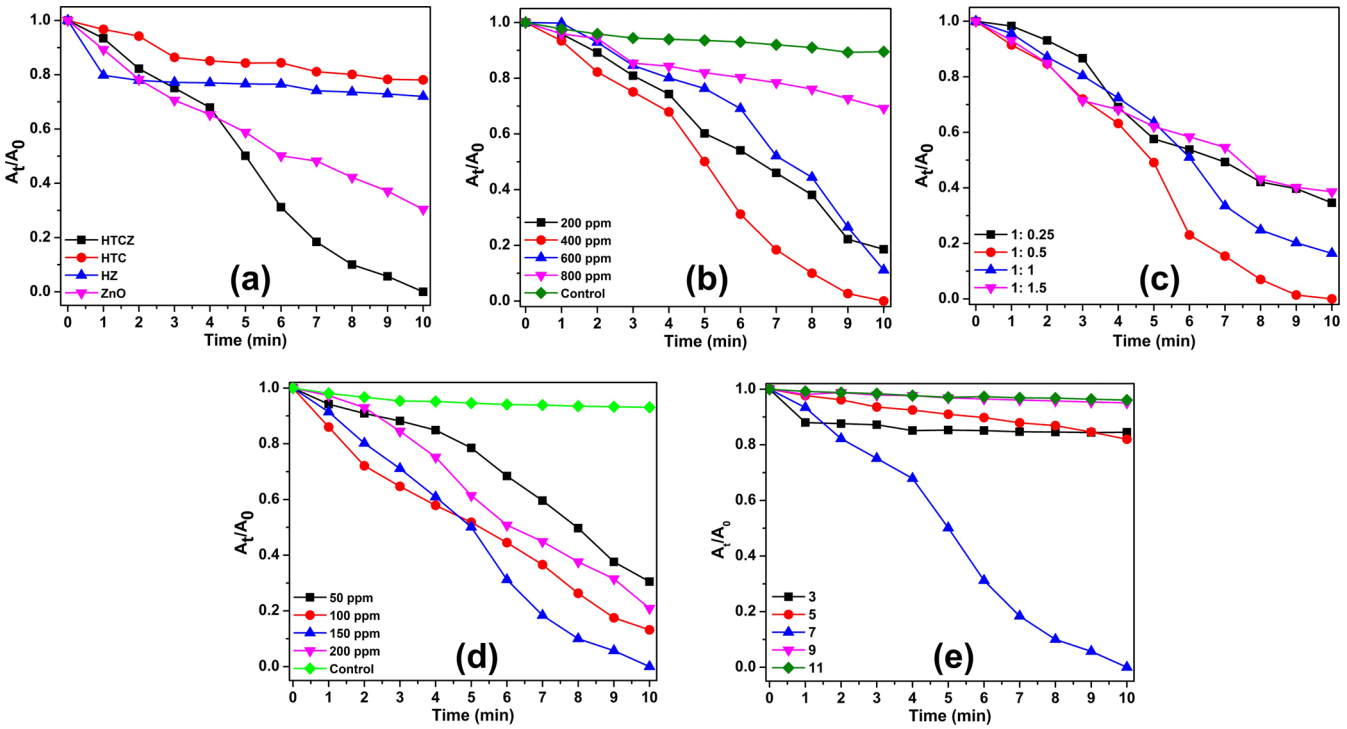

Figure 6. UV−vis optimization data for catalytic reduction of p-NP using different parameters such as (a) with different catalysts, (b) at different concentrations of Ti/Cu/Zn-HEG NCs, (c) ratios of various concentrations of ZnO to Ti/Cu-HEG NCs, (d) at different concentrations of p-NP and (e) at different pH values. Control represents the corresponding data with $NaBH_4$ in the absence of catalyst and p-NP in (b,d) respectively.

the lighter and darker portions in the colored representations. In HAADF analysis, the greater the *Z* value, the darker the depiction of that specific element, and vice versa. With a total magnification of 800 nm, the generated Ti/Cu/Zn-HEG NCs comprise darker and lighter Cu, Zn, Ti, O, and C hues, respectively. The EDS peak patterns of the formed elements adequately reflect the compositional examination of Ti/Cu/Zn-HEG NCs, which supports the tangible composite of the prepared NCs.

The results of an analysis using the Brunauer−Emmett−Teller (BET) and Barrett−Joyner−Halenda (BJH) models on the surface area and pore size distribution of Ti/Cu/Zn-HEG NCs are depicted in Figure 4a,b, respectively. The N_2 adsorption/desorption procedure utilized by the NCs is characterized as a Type V isotherm with an H3 hysteresis loop, as stated by IUPAC. The BET surface area was 39.026 m^2/g, but the relative pressure (P/P_0) was only 0.67−0.99. This behavior can be explained by weak adsorbent−adsorbate relationships, and molecular aggregation is often accompanied by pore filling at elevated pressures, resulting in increased surface area in the prepared NCs.[55,56] Furthermore, the pore width of Ti/Cu/Zn-HEG NCs at 7.05 nm in the BJH pore size distribution curve is typical of a mesopore-like material. Thus, Ti/Cu/Zn-HEG NCs are projected to have brilliant catalytic activity due to their large surface area and effective pore size.

To understand more about the surface charge and the feasibility of surface engineering concerning the reaction mechanism, X-ray photoelectron spectroscopy (XPS) is analyzed. This method also detects a material's surface properties, elemental content, and electronic states in the atom. The XPS spectrum of Ti/Cu/Zn-HEG NCs prepared sonochemically is shown in Figure 5a. Shirley's approach deconvolved all the peaks with the least distortion. The components discovered in the XPS spectrum correspond to the SEM-EDX results. Thus, Figure 5b displays C 1s spectra fragmented to multiple Lorentzian carbon peaks generated from H. It exhibits two significant peaks, one at 284.7 eV that can be attributed to the sp^2 (C═C) and sp^3 (C−C) hybridized graphitic carbon of C−C or C−H bonds, respectively, and another at 288.2 eV that can be related to the carboxyl (C═O) or ester (RCO_2R') connections.[57,58] Figure 5c describes the XPS data of Ti. Two important deconvoluted peaks at 458.2 eV of Ti $2p_{3/2}$ and 463.9 eV of Ti $2p_{1/2}$ electronic levels belong to Ti^{4+}, indicating Ti valence state to be +4.[59,60] The availability of Ti^{3+} ions in the material, leading to the production of O vacancies in the TiO_2 lattice, has been reported in the literature as satellite peaks.[61,62]

Meanwhile, the presence of metallic copper in the form of Cu^+ state can be verified by two intense peaks at 934.2 and 954.1 eV, which correlate to Cu $2p_{3/2}$ and Cu $2p_{1/2}$ states, respectively (Figure 5d). However, the appearance of two weaker satellite peaks at 942.8 and 962.0 eV implies that the Cu^{2+} chemical state is paramagnetic.[63−65] The XPS of Zn^{2+} $2p_{3/2}$ and Zn^{2+} $2p_{1/2}$ confirm the binding energy of ZnO with two prominent peaks at 1022.1 and 1045.2 eV, respectively, with no apparent shift in Figure 5e. O 1s photoelectron spectrum is wide and unsymmetrical, showcasing multivalent oxidation states with binding energies of 529.8 eV in Figure 5f. Some oxygen species are reported to be directly associated with these metal ions, whereas others are adsorbed on the surface.[66,67]

3.2. Investigation of Catalytic Activity. In a quartz cuvette with a capacity of 2 mL, the catalytic efficiency of Ti/Cu/Zn-HEG NCs was examined using the reduction of p-NP to p-AP as a model reaction. The reducing agent used in this experiment was $NaBH_4$. Using UV−vis spectroscopy (Agilent, Carry 100), the results of each of the reactions were plotted and recorded in Figure 6. Although p-NP exhibited a distinct

https://doi.org/10.1021/acsomega.3c03859
ACS Omega 2023, 8, 42164−42176

peak at 317 nm, the addition of $NaBH_4$ to the solution resulted in the production of a potent absorption peak at max = 400 nm. This phenomenon was observed, which could be accounted for by the appearance of yellow p-phenolate ions. On the other hand, a new peak was discovered at a maximum wavelength of 300 nm, which may result from the generation of *p*-aminophenol (p-AP) ions.[68,69] Aside from that, the performance of the reaction system was researched using only the catalyst and the $NaBH_4$. Besides, no induction period or resting phase was noted during the reaction. This interphase could be the time the catalyst takes to align its surface particles to improve different active sites.[7] As a result, the maximum time required to convert p-NP to p-AP using Ti/Cu/Zn-HEG NCs was approximately 10 min, which can be inferred toward the presence of multiple porous structures and active groups in the produced NCs. The optimization of several aspects and parameters is discussed in detail below.

Further, in Figure 6a, a comparison was made between Ti/Cu/Zn-HEG, Ti/Cu-HEG, Zn-HEG NCs, and ZnO NPs as catalysts for efficient conversion of p-NP. Despite the suitable environment, the catalyst Ti/Cu-HEG and Zn-HEG NCs could not form p-AP molecules in the reaction system. On the other hand, zinc oxide nanoparticles could convert p-NP although the process was slower. However, the transformation from p-NP to p-AP could be accomplished by Ti/Cu/Zn-HEG NCs in fewer than 10 min. This discovery might be due to the bigger pore size of the already synthesized Ti/Cu/Zn-HEG NCs, making it easier for p-NP molecules and borohydride ions to adsorb onto the catalyst's surface. This is supported by the findings of BJH, which show that, in contrast to NCs generated via other techniques, the pore diameter of Ti/Cu/Zn-HEG NCs builds considerably with the pore volume. This finding lends credence to the previous statement. This means that Ti/Cu/Zn-HEG NCs have greater catalytic activity in p-NP conversion than either Ti/Cu-HEG or Zn-HEG NCs alone. In addition, Figure S1a shows the control reaction that occurred when the experiment was conducted without Ti/Cu/Zn-HEG NCs.

Fast agglomeration could occur with an increase in catalyst concentration, which would reduce the efficiency of the catalytic process.[70] In the instance of 800 ppm Ti/Cu/Zn-HEG concentration, this might be the reason for the lowest yield in p-AP synthesis (Figure 6b). However, a delayed p-NP conversion was observed with catalyst concentrations of 200 and 600 ppm. The reaction was completed within 10 min after being catalyzed with 400 ppm of Ti/Cu/Zn-HEG NCs. The electron transmission from the donor (BH4) to the acceptor (p-NP) molecules was thought to have caused this conversion process. Control reactions (devoid of Ti/Cu/Zn-HEG NCs) have been investigated to enhance the qualitative outcomes.

Zinc oxide is known to be the most appropriate catalyst for reducing the time and temperature needed for organic synthesis and a way better adaption with other transition metals.[71] Thus, Figure 6c represents different concentration ratios of ZnO in Ti/Cu-HEG NC. With a low ratio of ZnO at 1:0.25, the conversion efficiency of p-NP is just 42% due to a lower content of ZnO molecules on the catalyst surface. However, the generation of p-AP was not so effective. It required more time for systematic channeling of electron movement when the ZnO concentration ratio was maintained at 1:1 and 1:1.5. In Ti/Cu-HEG NC, ~98% of p-NP converted when the ZnO concentration was held at 1:0.5.

p-NP conversion is often investigated at minimal concentrations. With a control reaction (without p-NP), we have reported roughly four initial p-NP concentrations in this publication, i.e., 50, 100, 150, and 200 ppm in Figure 6d. Due to the limiting presence of reactant molecules, no discernible conversion occurred at the lower p-NP concentrations of 50 and 100 ppm. The active sites of Ti/Cu/Zn-HEG NCs gradually fill up with p-NP molecules, until no more p-NP can be adsorbed. Therefore, it takes time for p-NP to convert at higher concentrations (200 ppm) completely. The optimized concentration for converting p-NP was chosen to be 150 ppm. The optimized concentration for converting p-NP was chosen to be 150 ppm. Moreover, the control reaction where the experiment was performed without $NaBH_4$ is displayed in Figure S1b.

From Figure 6e, it is evident that the highest rate of p-NP to p-AP conversion occurs at neutral pH = 7. Additional H^+ ions under acidic conditions may have hampered the chemical process at a lower pH. A similar pattern was also observed in basic pH. The possible justification could be a negative surface charge due to hydroxyl radicals in the system. The drop-in conversion rate was caused at higher pH, which the BH_4 might have brought on$^-$ ions and hydroxyl radicals repelling one another on the catalyst's surface. Thus, acidic and basic solution pH values could not promote the efficient conversion of p-NP.

3.3. Reaction Order and Rate Study. The procedure mentioned in Section 2.7 was followed to calculate the reaction and rate constant order, which are 1.5 and 0.092 min^{-1} $mg^{-0.5}$ $L^{0.5}$, respectively. Similar studies demonstrated the results to be on par with those obtained in this research (Figure 7).

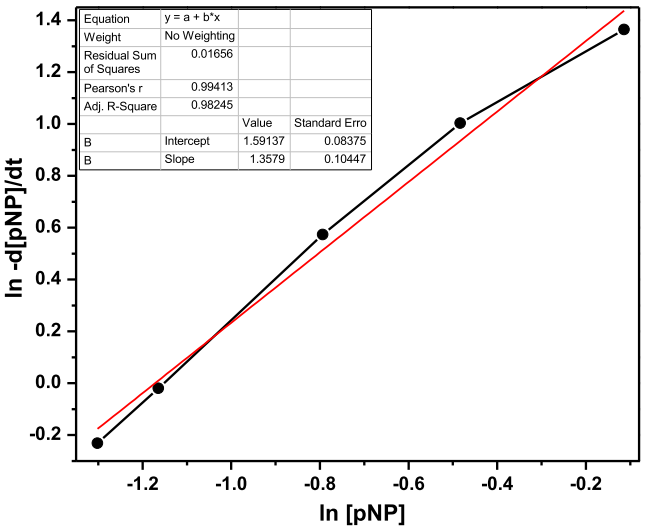

Figure 7. UV/vis kinetics data for the catalytic reduction of p-NP using Ti/Cu/Zn-HEG NCs.

3.4. Response Surface Methodology Used To Optimize the Process: ANOVA Analysis. Optimization of the response of an outcome variable influenced by multiple input elements can be achieved through the response surface method (RSM), also known as the response surface approach. Compared with other costly analysis methods like the finite element method or CFD analysis, this method is preferable because it allows for design optimization while simultaneously reducing total cost and numerical noise. However, the

https://doi.org/10.1021/acsomega.3c03859
ACS Omega 2023, 8, 42164−42176

Table 1. Parametric Coded Table Used for Design of the Experiment

factor	name	units	minimum	maximum	coded low (−1)	coded high (+1)	mean	std. dev.
A	catalyst conc	ppm	100	300	150	250	200	45.88
B	p-NP conc	ppm	50	250	100	200	150	45.88
C	pH		5	9	6	8	7	0.9177

technique is more difficult because of the wide range of coefficient estimate values that can result from the impact of each parameter on output variables and the interacting effect of each parameter on outcome variables when the responses are independent of one another. The most common RSM methods used in design experiments are the Central Composite design (CCD), Box-Behnken, and Doehlert designs.[30,72−76]

The statistical plan offered by Design Expert Software (Version 6.0, Stat-Ease, Minneapolis, USA) was utilized in each of our experiments. It was hypothesized that several factors, such as pH, the concentration of the catalyst in parts per million, and the concentration of the p-nitrophenol in parts per million, all affected the conversion efficiency of p-NP to p-AP. To put it another way, this is the typical response produced by the central composite design procedure. To be more specific, the lowest and highest values for catalyst concentration (ppm), p-NP concentration (ppm), and pH, respectively, were decided to be 100, 50, and 5. Tables 1 and 2 display the parametric coded table developed by Design Expert Software and the statistical experimental design. The effectiveness of the experimental design was evaluated with the help of the model, which considered a variety of factors.

Table 2. Statistical Experimental Design Generated from RSM

		factor 1	factor 2	factor 3	responses	
std	run	A: catalyst conc. (ppm)	B: p-NP conc. (ppm)	C: pH	observed conversion efficiency (%)	predicted conversion efficiency (%)
7	1	150	200	8	78	76.8
9	2	100	150	7	62	61.9
11	3	200	50	7	80	80.4
16	4	200	150	7	98	97.2
10	5	300	150	7	45	45.4
14	6	200	150	9	90	90.8
2	7	250	100	6	82	82.6
3	8	150	200	6	85	86.1
18	9	200	150	7	98	99.1
6	10	250	100	8	84	83.1
5	11	150	100	8	74	75.2
20	12	200	150	7	98	98.5
13	13	200	150	5	85	85.2
17	14	200	150	7	98	98.2
1	15	150	100	6	80	80.7
8	16	250	200	8	70	68.4
12	17	200	250	7	68	69.4
19	18	200	150	7	98	98.4
4	19	250	200	6	65	66.4
15	20	200	150	7	98	97.4

Among the many RSM techniques, the CCD methodology lends itself to designing experiments the most effectively. It is made up of factorial runs, axial runs, and center runs, for the most part. The following equation can be used to determine how many trials need to be conducted for each of the different process variables:

$$N = 2^n + 2n + n_c = 2^3 + (2 \times 3) + 8 = 20$$

where N represents the required total number of experiments and the total number of variables that are considered independent. The CCD method necessitates three stages: first, the execution of design tests; second, the calculation of model coefficients; and third, the forecasting of model behavior and acceptance. As a result, a simulation model is created to calculate behavior based on input process variables and their interactions. The quadratic regression model equation allows for process actions:

$$Y = b_0 + \sum_{i=1}^{k} b_i X_i + \sum_{i=1}^{k} b_{ii} X_i^2 + \sum_{i=1}^{k-1} \sum_{j=2}^{k} b_{ii} X_i X_j \quad (4)$$

where b_i is a linear coefficient, b_{ii} and b_{ij} are interactive and quadratic coefficients, and b_0 is a constant.[77] The amounts of and were considered when accepting the polynomial model equation. Higher correlation coefficients improved experimental data fitting to the proposed polynomial equation.

The regression model used all three factors (catalyst concentration, ppm; p-NP concentration, ppm, and pH) as input variables with p-NP to p-AP conversion efficiency. The statistical coefficients were calculated using Design Expert Software 6.0, as stated in eq 5:

$$\begin{aligned}\text{Conversion efficiency (\%)} &= -234.90909 + 1.68205(\text{Catalyst conc.}) \\ &\quad + 1.03841(\text{p-NP conc.}) + 27.52273(\text{pH}) \\ &\quad - 0.002000(\text{Catalyst conc.})(\text{p-NP conc.}) \\ &\quad + 0.050000(\text{Catalyst conc.})(\text{pH}) + 0.005000 \\ &\quad (\text{p-NP conc.})(\text{pH}) - 0.004486(\text{Catalyst conc.})^2 \\ &\quad - 0.002436(\text{p-NP conc.})^2 - 2.71591(\text{pH})^2 \end{aligned} \quad (5)$$

As all of these parameters are interconnected, all process parameters were crucial for the design experiment.

To identify significant regression model equation parameters, ANOVA was used. F-test analysis was used throughout the multifaceted research project. F and P values that are either greater or lower than the coefficient values should be observed. When the sum of squares is quite high, the relevance of any process variable is proportionally and noticeably increased. If the P value is less than 0.0001, then the sum of squares is 3524.34. The mean square value of 1174.78, the value of the standard deviation of 2.07, the value of F of 105.36, the mean value of 81.80, and the CV (%) value of 2.53 indicate that the model is significant. The conjugate diagram illustrating the efficiency of converting p-NP to p-AP utilizing Ti/Cu/Zn-HEG NCs is illustrated in several distinct figures (Figure 8a−

https://doi.org/10.1021/acsomega.3c03859
ACS Omega 2023, 8, 42164−42176

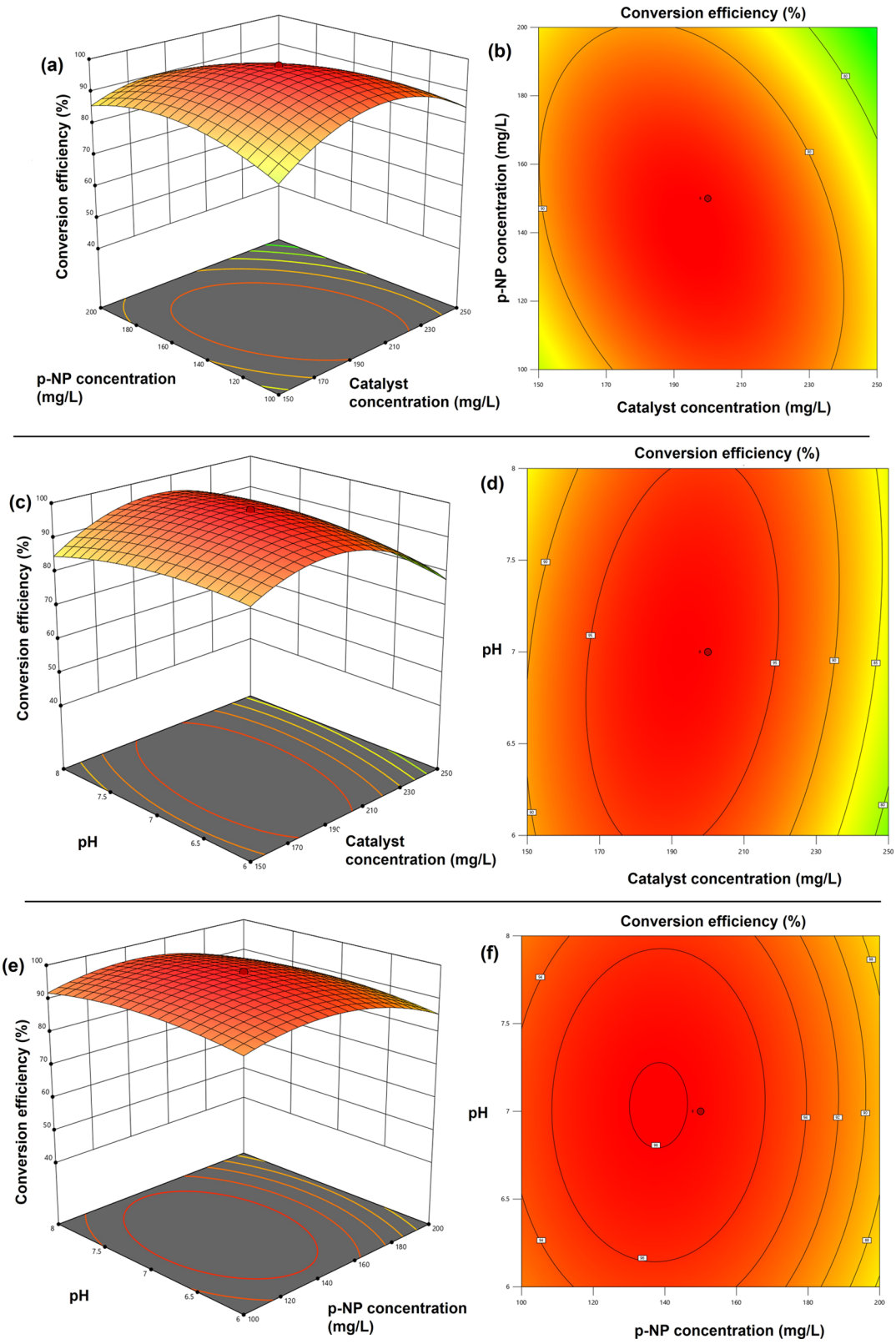

Figure 8. Response surface plot diagrams showing variation of conversion efficiency % of p-NP with variable parameters: (a,b) 3D and contour plots on conjugated effects of p-NP concentration and catalyst concentration on p-NP conversion; (c,d) 3D and contour plots on conjugated effects of pH and catalyst concentration on p-NP conversion; (e,f) 3D and contour plots on conjugated effects of pH and p-NP concentration on p-NP conversion.

f). Calculating the initial and end concentrations of p-NP and p-AP in the solution, respectively, and the projected values using a mathematical model equation developed by CCD allowed for the derivation of the actual results. Both actual and predicted data were utilized in the calculation of the overall model's correlation coefficient (R^2), which was then expressed

https://doi.org/10.1021/acsomega.3c03859
ACS Omega 2023, 8, 42164−42176

in terms of the adjusted correlation coefficient (0.98), as well as the expected correlation coefficient (0.91).

Figure 8a depicts the combination plot of catalyst concentration and p-NP concentration versus conversion efficiency at a constant pH. Maximum conversion efficiency (90%) is achieved at a catalyst concentration of 220 ppm and a p-NP concentration of 16 ppm when both the preliminary catalyst concentration and the p-NP concentration are increased from 150 to 250 ppm and 100 to 200 ppm, respectively. After that point, the conversion efficiency began to rise for both components, and it continued to rise until the components reached their respective maximum concentrations (250 and 200 ppm). Figure 8c depicts the interaction between the catalyst concentration and pH on conversion efficiency. The conversion efficiency went from 50 to 90% when the initial catalyst concentration was raised from 150 to 220 ppm. Beyond 220 ppm of catalyst initially, the conversion efficiency started to drop from 90 to 77%. Concurrently, the conversion efficiency increased from 50 to 84% when the pH was raised from 6 to 8. At a fixed starting concentration of p-NP, both associated effects were observed. The coupled effects of pH and p-NP concentration on the p-NP to p-AP conversion efficiency are shown in Figure 8e. When the p-NP concentration increases from 100 to 160 ppm, the conversion efficiency increases from 55 to 92%. However, when the p-NP concentration is increased further than 160 mg/L, the maximum efficiency falls from 92 to 86%.

On the other hand, the pH level must be raised from 6 to 8 to improve the conversion efficiency from 55 to 92%. The contour plots of all the effective parameters are depicted in Figure 8b,d,f, respectively. The contour graphs are projections of the three-dimensional plots onto the two-dimensional plot. This plot in two dimensions depicts the maximum and lowest points on a three-dimensional graph and the effect of two factors on a particular response. The maximum conversion efficiency of 98% was attained at the pH value of 7 and the catalyst concentration dose of 200 ppm. The initial p-NP concentration was set to 150 ppm. Since the attractiveness value of the model is 1, it can be concluded that it is suitable for analyzing the design experiment.

3.5. Error Analysis for the Prediction of Model Accuracy. The predicted response from the RSM model and observed response obtained from experimental investigations are presented in Table 2. The ability of RSM models was evaluated statistically through the determination of coefficient of determination (R^2), relative error (RE), and Willmott d-index ($d_{\text{will-index}}$) values, which are described below:

(i) The model-derived data and the experimentally observed data were used in the error analysis that was performed using a standard statistical method known as the relative error analysis (Table 2). This method consisted of evaluating certain parameters per the following list of criteria:

(a) Root-mean-square error (RMSE) was computed by

$$\text{RMSE} = \left[\sum_{N=1}^{n} \frac{(P_N - E_N)^2}{N}\right]^{1/2} \quad (6)$$

where E_N and P_N are the values of experimental findings and model-predicted data.

(b) Relative error (RE) was then measured as

$$\text{RE} = (\text{RMSE}/E_{\text{mean}}) \quad (7)$$

where E_{mean} is the mean value of experimental data.

(ii) In order to improve the performance of the model, it is attainable to assess the model using the Willmott d-index ($d_{\text{will-index}}$) method, which was evaluated in the following way:

$$d_{\text{index}} = \left[1 - \frac{\sum_{N=1}^{n} (P_N - E_N)^2}{\sum_{N=1}^{n} [|(P_N - E_{\text{mean}})| + |(E_N - E_{\text{mean}})|]^2}\right] \quad (8)$$

(iii) The following expression was used to determine the value of the regression coefficient (R^2):

$$R^2 = \frac{A_{xy}{}^2}{P_x{}^2 P_y{}^2} \quad (9)$$

where $A_{xy}{}^2$ is the covariance of the independent and dependent variables and $P_x{}^2$ and $P_y{}^2$ are the variances of the independent and dependent variables, respectively.

In terms of relative errors (RE), regression coefficients (R^2), and Willmott d-index (d_{index}), the developed model predicts integrated system performance well. The relative error was 0.097 using the experimental data and the model's predicted data. In contrast, the regression coefficient (R^2) and Willmott d-index ($d_{\text{will-index}}$) were found to be 0.975 and 0.966, respectively. Less relative error and high values for the regression coefficient ($R^2 > 0.97$) and Willmott d-index ($d_{\text{will-index}} > 0.95$) reflect the model's excellent agreement with the experimental data.

3.6. Reusability Potential of Ti/Cu/Zn-HEG NCs. After the catalytic conversion of p-NP to p-AP, the reusability potential of the Ti/Cu/Zn-HEG NCs was examined. Following the procedure outlined in the experimental section, the catalyst was collected and used for three additional cycles. The conversion process took approximately the same amount of time as the catalyst's initial utilization, as seen in Figure 9. But when it was employed in the fourth and fifth cycles, the entire conversion procedure took an additional 2−5 min. This

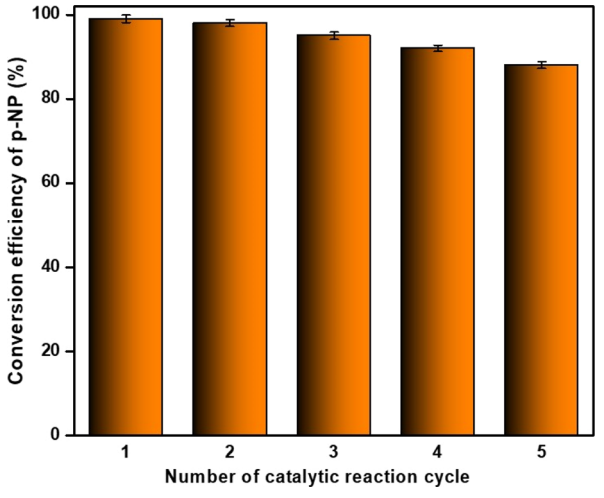

Figure 9. Conversion efficiency of p-NP (%) with respect to number of reaction cycles in over Ti/Cu/Zn-HEG NCs (catalyst loading = 400 ppm).

https://doi.org/10.1021/acsomega.3c03859
ACS Omega 2023, 8, 42164−42176

implied that Ti/Cu/Zn-HEG NCs are quite stable materials that may be recycled at least three times without significantly losing their catalytic characteristics, lessening the process's economic strain.[20,37]

4. CONCLUSIONS

In conclusion, we successfully synthesized Ti/Cu/Zn-HEG NCs using in situ sonochemical coprecipitation with a two-step approach. The resulting material exhibited characteristic peaks of hydrogen exfoliated graphene (HEG), Ti/Cu-HEG, and ZnO, along with the formation of exfoliated sheets in a layered structure after undergoing thermal treatment at 500 °C. Transmission electron microscopy (TEM) analysis revealed the evidence of well-defined NCs in the size range of 20−30 nm. Furthermore, X-ray photoelectron spectroscopy (XPS) analysis provided quantitative data confirming the distribution of ions in the material. The Brunauer−Emmett−Teller and Barrett−Joyner−Halenda (BET−BJH) analysis demonstrated that Ti/Cu/Zn-HEG NCs possessed a nanoporous structure, boasting a large surface area and pore volume—a promising characteristic for catalytic applications. Assessing the catalytic activity of Ti/Cu/Zn-HEG NCs, we investigated their performance in the reduction of p-nitrophenol (p-NP) in the presence of an excess of NaBH4. The catalytic reduction reaction was found to be approximately of 1.5 order, with a calculated rate constant of k_{app} = 0.092 min^{-1} $mg^{-0.5}$ $L^{0.5}$. Optimal conditions for maximum p-NP degradation were achieved with a p-NP concentration of 150 ppm, a catalyst concentration of 400 ppm, and a total reaction time of 10 min. One notable advantage of the newly synthesized material is its recyclability without a significant loss of catalytic activity, making it a promising candidate for commercial-scale applications in the chemical processing industries. The potential of Ti/Cu/Zn-HEG NCs lies in their efficient catalytic performance, nanoporous structure, and ability to contribute to environmentally friendly and sustainable processes. These findings pave the way for the further exploration and utilization of these NCs in various industrial applications.

■ ASSOCIATED CONTENT

Supporting Information

The Supporting Information is available free of charge at https://pubs.acs.org/doi/10.1021/acsomega.3c03859.

Control reactions for conversion of p-NP to p-AP (PDF)

■ AUTHOR INFORMATION

Corresponding Authors

Fatimah Othman Alqahtani − *Department of Chemistry, College of Science, King Faisal University, Al-Ahsa 31982, Saudi Arabia*; Email: Foqahtani@kfu.edu.sa

Byong-Hun Jeon − *Department of Earth Resources & Environmental Engineering, Hanyang University, Seoul 04763, Republic of Korea*; Email: bhjeon@hanyang.ac.kr

Suraj K Tripathy − *School of Chemical Technology, Kalinga Institute of Industrial Technology, Bhubaneswar, Odisha 751024, India*; Email: suraj.tripathy@kiitbiotech.ac.in

Authors

Meerambika Behera − *School of Chemical Technology, Kalinga Institute of Industrial Technology, Bhubaneswar, Odisha 751024, India*

Sankha Chakrabortty − *School of Chemical Technology, Kalinga Institute of Industrial Technology, Bhubaneswar, Odisha 751024, India*; orcid.org/0000-0001-7719-8586

Jayato Nayak − *Centre for Life Science, Mahindra University, Hyderabad, Telangana 500043, India*

Shirsendu Banerjee − *School of Chemical Technology, Kalinga Institute of Industrial Technology, Bhubaneswar, Odisha 751024, India*

Ramesh Kumar − *Department of Earth Resources & Environmental Engineering, Hanyang University, Seoul 04763, Republic of Korea*

Complete contact information is available at: https://pubs.acs.org/10.1021/acsomega.3c03859

Author Contributions

⊥M.B., F.O.A., and S.C. contributed equally.

Notes

The authors declare no competing financial interest.

■ ACKNOWLEDGMENTS

This work was supported by the National Research Foundation of Korea (NRF) grant funded by the Korea government (MSIT) (No. RS-2023-00219983). S.C. acknowledges the University Grants Commission, Government of India, under the UGC-FRPS scheme (Project No. F.30-575/2021). One of the authors (R.K.) acknowledges the financial support through the Creative and Challenging Research Program (grant no. 2021R1I1A1A01060846) of the National Research Foundation (NRF) of the Republic of Korea.

■ REFERENCES

(1) *The Outlook For Energy: A View To 2040*. Clim Positions 2015.

(2) Kumar, R.; Ghosh, A. K.; Pal, P. Sustainable Production of Biofuels through Membrane-Integrated Systems. *Sep. Purif. Rev.* **2020**, *49* (3), 207−228.

(3) Friend, C. M.; Xu, B. Heterogeneous Catalysis: A Central Science for a Sustainable Future. *Acc. Chem. Res.* **2017**, *50*, 517−521.

(4) Schlögl, R. Heterogeneous catalysis. *Angew. Chem., Int. Ed. Engl.* **2015**, *54*, 3465−3520.

(5) Xu, Y.; Cao, M.; Zhang, Q. Recent advances and perspective on heterogeneous catalysis using metals and oxide nanocrystals. *Mater. Chem. Front* **2021**, *5*, 151−222.

(6) Hervés, P.; Pérez-Lorenzo, M.; Liz-Marzán, L. M.; Dzubiella, J.; Lub, Y.; Ballauff, M. Catalysis by metallic nanoparticles in aqueous solution: model reactions. *Chem. Soc. Rev.* **2012**, *41*, 5577−5587.

(7) Tchieno, F. M. M.; Tonle, I. K.; P-Nitrophenol determination and remediation: An overview. *Rev. Anal. Chem.* **2018**; *37* doi: .

(8) 4-Nitrophenol in freshwater and marine water n.d. https://www.waterquality.gov.au/anz-guidelines/guideline-values/default/water-quality-toxicants/toxicants/4-nitrophenol-2000 (accessed Mar 22, 2023).

(9) 4-Nitrophenol Hazard Summary, https://www.epa.gov/sites/default/files/2016-09/documents/4-nitrophenol.pdf (accessed Jan 15, 2023).

(10) Pradhan, N.; Pal, A.; Pal, T. Catalytic reduction of aromatic nitro compounds by coinage metal nanoparticles. *Langmuir* **2001**, *17*, 1800−1802.

(11) Formenti, D.; Ferretti, F.; Scharnagl, F. K.; Beller, M. Reduction of Nitro Compounds Using 3d-Non-Noble Metal Catalysts. *Chem. Rev.* **2019**, *119*, 2611−2680.

(12) Védrine, J. C. Heterogeneous Catalysis on Metal Oxides. *Catalysts* 2017, *7*, 341, DOI: 10.3390/CATAL7110341.

(13) Wang, Y.; Arandiyan, H.; Scott, J.; Bagheri, A.; Dai, H.; Amal, R. Recent advances in ordered meso/macroporous metal oxides for

heterogeneous catalysis: a review. *J. Mater. Chem. A* **2017**, *5*, 8825−8846.
(14) Vedrine, J. C. mportance, features and uses of metal oxide catalysts in heterogeneous catalysis. *Chin. J. Catal.* **2019**, *40*, 1627−1636.
(15) Wu, G.; Liang, X.; Zhang, L.; Tang, Z.; Al-Mamun, M.; Zhao, H. Fabrication of Highly Stable Metal Oxide Hollow Nanospheres and Their Catalytic Activity toward 4-Nitrophenol Reduction. *ACS Appl. Mater. Interfaces* **2017**, *9*, 18207−18214.
(16) Behera, M.; Tiwari, N.; Basu, A.; Mishra, S. R.; Banerjee, S.; Chakrabortty, S.; Tripathy, S. K. Maghemite/ZnO nanocomposites: A highly efficient, reusable and non-noble metal catalyst for reduction of 4-nitrophenol. *Adv. Powder Technol.* **2021**, *32*, 2905−2915.
(17) Jacob, B.; Mohan, M.; Dhanyaprabha, K. C.; Thomas, H. $NiCo_2O_4$ nanoparticles anchored on reduced graphene oxide with enhanced catalytic activity towards the reduction of p-Nitrophenol in water. *Colloids Surf., A* **2022**, *643*, No. 128717.
(18) Guo, H.; Yang, H.; Huang, J.; Tong, J.; Liu, X.; Wang, Y. Theoretical and experimental insight into plasma-catalytic degradation of aqueous p-nitrophenol with graphene-ZnO nanoparticles. *Sep. Purif. Technol.* **2022**, *295*, No. 121362.
(19) Kumar, R.; Pal, P. Response surface-optimized Fenton's pretreatment for chemical precipitation of struvite and recycling of water through downstream nanofiltration. *Chem. Eng. J.* **2012**, *210*, 33−44.
(20) Kumar, R.; Liu, C.; Ha, G.-S.; Kim, K. H.; Chakrabortty, S.; Tripathy, S. K.; Park, Y.-K.; Khan, M. A.; Yadav, K. K.; Cabral-Pinto, M. M. S.; et al. A novel membrane-integrated sustainable technology for downstream recovery of molybdenum from industrial wastewater. *Resour., Conserv. Recycl.* **2023**, *196*, No. 107035.
(21) Kumar, R.; Pal, P. Lipase immobilized graphene oxide biocatalyst assisted enzymatic transesterification of *Pongamia pinnata* (Karanja) oil and downstream enrichment of biodiesel by solar-driven direct contact membrane distillation followed by ultrafiltration. *Fuel Process. Technol.* **2021**, *211*, No. 106577.
(22) Kumar, R.; Kim, T. H.; Basak, B.; Patil, S. M.; Kim, H. H.; Ahn, Y.; Yadav, K. K.; Cabral-Pinto, M. M. S.; Jeon, B.-H. Emerging approaches in lignocellulosic biomass pretreatment and anaerobic bioprocesses for sustainable biofuels production. *J. Clean. Prod.* **2022**, *333*, No. 130180.
(23) Shen, K.; Xue, X.; Wang, X.; Hu, X.; Tian, H.; Zheng, W. One-step synthesis of band-tunable N, S co-doped commercial TiO2/graphene quantum dots composites with enhanced photocatalytic activity. *RSC Adv.* **2017**, *7* (38), 23319−23327.
(24) Shen, J.; Hu, Y.; Li, C.; Qin, C.; Shi, M.; Ye, M. Layer-by-layer self-assembly of graphene nanoplatelets. *Langmuir* **2009**, *25* (11), 6122−6128.
(25) Zhang, F.; Hou, C.; Zhang, Q.; Wang, H.; Li, Y. Graphene sheets/cobalt nanocomposites as low-cost/high-performance catalysts for hydrogen generation. *Mater. Chem. Phys.* **2012**, *135* (2−3), 826−831.
(26) Huang, X.; Qi, X.; Boey, F.; Zhang, H. Graphene-based composites. *Chem. Soc. Rev.* **2012**, *41* (2), 666−686.
(27) Huang, X.; Yin, Z.; Wu, S.; Qi, X.; He, Q.; Zhang, Q.; Yan, Q.; Boey, F.; Zhang, H. Graphene-based materials: synthesis, characterization, properties, and applications. *Small* **2011**, *7* (14), 1876−1902.
(28) Mullen, K. Evolution of graphene molecules: structural and functional complexity as driving forces behind nanoscience. *ACS Nano* **2014**, *8* (7), 6531−6541.
(29) Zhu, Y.; Kong, G.; Pan, Y.; Liu, L.; Yang, B.; Zhang, S. An improved Hummers method to synthesize graphene oxide using much less concentrated sulfuric acid. *Chin. Chem. Lett.* **2022**, *33*, 4541−4544.
(30) Chakrabortty, S.; Nayak, J.; Pal, P.; Kumar, R.; Banerjee, S.; Mondal, P. K. Catalytic conversion of CO2 to biofuel (methanol) and downstream separation in membrane-integrated photoreactor system under suitable conditions. *Int. J. Hydrogen Energy* **2020**, *45*, 675−690.
(31) Ama, O. M.; Arotiba, O. A. Exfoliated graphite/titanium dioxide for enhanced photoelectrochemical degradation of methylene blue dye under simulated visible light irradiation. *J. Electroanal. Chem.* **2017**, *803*, 157−164.
(32) de Luna, M. D. G.; Garcia-Segura, S.; Mercado, C. H.; Lin, Y. T.; Lu, M. C. Doping TiO2 with CuSO4 enhances visible light photocatalytic activity for organic pollutant degradation. *Environ. Sci. Pollut. Res.* **2020**, *27*, 24604−24613.
(33) Basu, A.; Misra, A. J.; Behera, M.; Behera, S. K.; Nayak, A. K.; Dhal, N. K. Photocatalytic disinfection of extended-spectrum beta-lactamase producing Escherichia coli using Alumina/ZnO heterostructures. *J. Environ. Chem. Eng.* **2021**, *9*, No. 106334.
(34) Dash, S.; Das, S.; Khan, M. I.; Sinha, S.; Das, B.; Jayabalan, R. Sonochemically synthesized Ag/CaCO3 nanocomposites: A highly efficient reusable catalyst for reduction of 4-nitrophenol. *Mater. Chem. Phys.* **2018**, *220*, 409−416.
(35) Pozun, Z. D.; Rodenbusch, S. E.; Keller, E.; Tran, K.; Tang, W.; Stevenson, K. J. A systematic investigation of p -nitrophenol reduction by bimetallic dendrimer encapsulated nanoparticles. *J. Phys. Chem. C* **2013**, *117*, 7598−7604.
(36) Denrah, S.; Sarkar, M. Design of experiment for optimization of nitrophenol reduction by green synthesized silver nanocatalyst. *Chem. Eng. Res. Des.* **2019**, *144*, 494−504.
(37) Behera, M.; Tiwari, N.; Banerjee, S.; Sheik, A. R.; Kumar, M.; Pal, M. Ag/biochar nanocomposites demonstrate remarkable catalytic activity towards reduction of p-nitrophenol via restricted agglomeration and leaching characteristics. *Colloids Surf., A* **2022**, *642*, No. 128616.
(38) Flores-Vélez, L. M.; Domínguez, O.; Flores-Vélez, L. M.; Domínguez, O. Graphene Oxide/Multilayer-Graphene Synthesized from Electrochemically Exfoliated Graphite and Its Influence on Mechanical Behavior of Polyurethane Composites. *Mater. Sci. Appl.* **2018**, *9*, 565−575.
(39) Guo, Y.; Liu, J.; Xu, Y. T.; Zhao, B.; Wang, X.; Fu, X. Z. In situ redox growth of mesoporous Pd-Cu2O nanoheterostructures for improved glucose oxidation electrocatalysis. *Sci. Bull.* **2019**, *64*, 764−773.
(40) Chenari, H. M.; Seibel, C.; Hauschild, D.; Reinert, F.; Abdollahian, H. Titanium Dioxide Nanoparticles: Synthesis, X-Ray Line Analysis and Chemical Composition Study. *Mater. Res.* **2016**, *19*, 1319−1323.
(41) Chougala, L. S.; Yatnatti, M. S.; Linganagoudar, R. K.; Kamble, R. R.; Kadadevarmath, J. S. A Simple Approach on Synthesis of TiO_2 Nanoparticles and its Application in dye Sensitized Solar Cells. *J. Nano- Electron. Phys.* **2017**, *9*, 4005.
(42) Kalaiarasi, S.; Jose, M. Dielectric functionalities of anatase phase titanium dioxide nanocrystals synthesized using water-soluble complexes. *Appl. Phys. A: Mater. Sci. Process.* **2017**, *123*, 152.
(43) Narushima, T.; Tsukamoto, H.; Yonezawa, T. High temperature oxidation event of gelatin nanoskin-coated copper fine particles observed by in situ TEM. *AIP Adv.* **2012**, *2*, No. 042113.
(44) Raffi, M.; Mehrwan, S.; Bhatti, T. M.; Akhter, J. I.; Hameed, A.; Yawar, W. Investigations into the antibacterial behavior of copper nanoparticles against *Escherichia coli*. *Ann. Microbiol.* **2010**, *60*, 75−80.
(45) Muhammad, W.; Ullah, N.; Haroon, M.; Abbasi, B. H. Optical, morphological and biological analysis of zinc oxide nanoparticles (ZnO NPs) using Papaver somniferum L. *RSC Adv.* **2019**, *9*, 29541−29548.
(46) Nagaraju, G.; Udayabhanu, S.; Prashanth, S. A.; Shastri, M.; Yathish, K. V. Electrochemical heavy metal detection, photocatalytic, photoluminescence, biodiesel production and antibacterial activities of Ag−ZnO nanomaterial. *Mater. Res. Bull.* **2017**, *94*, 54−63.
(47) Anupama, C.; Kaphle, A.; Udayabhanu; Nagaraju, G. Aegle marmelos assisted facile combustion synthesis of multifunctional ZnO nanoparticles: study of their photoluminescence, photo catalytic and antimicrobial activities. *J. Mater. Sci. Mater. Electron.* **2018**, *29*, 4238−4249.
(48) Wang, J.; Wang, M.; Xiong, J. R.; Lu, C. H. Enhanced photocatalytic activity of a TiO2/graphene composite by improving the reduction degree of graphene. *New Carbon Mater.* **2015**, *30*, 357−363.

https://doi.org/10.1021/acsomega.3c03859
ACS Omega 2023, 8, 42164−42176

(49) Alswat, A. A.; Ahmad, M.; Bin; Saleh, T. A. Preparation and Characterization of Zeolite\Zinc Oxide-Copper Oxide Nanocomposite: Antibacterial Activities. *Colloid Interface Sci. Commun.* **2017**, *16*, 19−24.
(50) Hitkari, G.; Chowdhary, P.; Kumar, V.; Singh, S.; Motghare, A. Potential of Copper-Zinc Oxide nanocomposite for photocatalytic degradation of congo red dye. *Clean Chem. Eng.* **2022**, *1*, No. 100003.
(51) Mehta, M.; Chandrabose, G.; Krishnamurthy, S.; Avasthi, D. K.; Chowdhury, S. Improved photoelectrochemical properties of TiO2-graphene nanocomposites: Effect of defect induced visible light absorption and graphene conducting channel for carrier transport. *Appl. Surf. Sci. Adv.* **2022**, *11*, No. 100274.
(52) Ahmed, Alshehri N.; Assaifan, A. K.; Albalawi, A. A.; Alghamdi, E. H.; Niu, Y.; Pleydell-Pearce, C. Fabrication and characterisation of ZnO@TiO2 core/shell nanowires using a versatile kinetics-controlled coating growth method. *Appl. Surf. Sci.* **2022**, *594*, No. 153463.
(53) Tobaldi, D. M.; Lajaunie, L.; Dvoranová, D.; Brezová, V.; Figueiredo, B.; Seabra, M. P. Cooperative and fully reversible color switching activation in hybrid graphene decorated nanocages and copper-TiO2 nanoparticles. *Mater. Today Energy* **2020**, *17*, No. 100460.
(54) Sadeghian, Z.; Hadidi, M. R.; Salehzadeh, D.; Nemati, A. Hydrophobic octadecylamine-functionalized graphene/TiO2 hybrid coating for corrosion protection of copper bipolar plates in simulated proton exchange membrane fuel cell environment. *Int. J. Hydrogen Energy* **2020**, *45*, 15380−15389.
(55) Ossonon, B. D.; Bélanger, D. Synthesis and characterization of sulfophenyl-functionalized reduced graphene oxide sheets. *RSC Adv.* **2017**, *7*, 27224−27234.
(56) Ambroz, F.; Macdonald, T. J.; Martis, M. V.; Parkin, I. P.; Ambroz, F.; Macdonald, T. J. Evaluation of the BET Theory for the Characterization of Meso and Microporous MOFs. *Small Methods* **2018**, *2*, No. 1800173.
(57) Dolgov, A.; Lopaev, D.; Lee, C. J.; Zoethout, E.; Medvedev, V.; Yakushev, O. Characterization of carbon contamination under ion and hot atom bombardment in a tin-plasma extreme ultraviolet light source. *Appl. Surf. Sci.* **2015**, *353*, 708−713.
(58) Kim, C. K.; Choi, I. T.; Kang, S. H.; Kim, H. K. Anchovy-derived nitrogen and sulfur co-doped porous carbon materials for high-performance supercapacitors and dye-sensitized solar cells. *RSC Adv.* **2017**, *7*, 35565−35574.
(59) Xie, W.; Li, R.; Xu, Q. Enhanced photocatalytic activity of Se-doped TiO_2 under visible light irradiation. *Sci. Rep.* **2018**, *8*, 8752.
(60) Zhang, H.; Han, Y.; Yang, L.; Guo, X.; Wu, H.; Mao, N. Photocatalytic Activities of PET Filaments Deposited with N-Doped TiO_2 Nanoparticles Sensitized with Disperse Blue Dyes. *Catalysts* **2020**, *10*, 531.
(61) Bharti, B.; Kumar, S.; Lee, H. N.; Kumar, R. Formation of oxygen vacancies and Ti3+ state in TiO_2 thin film and enhanced optical properties by air plasma treatment. *Sci. Rep.* **2016**, *6*, 32355.
(62) Janczarek, M.; Kowalska, E. Defective Dopant-Free TiO_2 as an Efficient Visible Light-Active Photocatalyst. *Catalysts* **2021**, *11*, 978.
(63) Yu, J.; Ran, J. Facile preparation and enhanced photocatalytic H_2-production activity of $Cu(OH)_2$ cluster modified TiO_2. *Energy Environ. Sci.* **2011**, *4*, 1364−1371.
(64) Jin, Z.; Liu, C.; Qi, K.; Cui, X. Photo-reduced Cu/CuO nanoclusters on TiO_2 nanotube arrays as highly efficient and reusable catalyst. *Sci. Rep.* **2017**, *7*, 39695.
(65) Swadźba-Kwaśny, M.; Chancelier, L.; Nag, S.; Manyar, H. G.; Hardacre, C.; Nockemann, P. Facile in situ synthesis of nanofluids based on ionic liquids and copper oxide clusters and nanoparticles. *Dalton Trans.* **2011**, *41*, 219−1227.
(66) Huang, C.; Ye, W.; Liu, Q.; Qiu, X. Dispersed Cu_2O Octahedrons on h-BN Nanosheets for p-Nitrophenol Reduction. *ACS Appl. Mater. Interfaces* **2014**, *6*, 14469−14476.
(67) Mi, Y.; Wen, L.; Xu, R.; Wang, Z.; Cao, D.; Fang, Y. Constructing a AZO/TiO_2 Core/Shell Nanocone Array with Uniformly Dispersed Au NPs for Enhancing Photoelectrochemical Water Splitting. *Adv. Energy Mater.* **2016**, *6*, No. 1501496.
(68) Zhang, M.; Chen, X.; Zhou, H.; Murugananthan, M.; Zhang, Y. Degradation of p-nitrophenol by heat and metal ions co-activated persulfate. *Chem. Eng. J.* **2015**, *264*, 39−47.
(69) Zhao, C.; Xue, L.; Shi, H.; Chen, W.; Zhong, Y.; Zhang, Y. Simultaneous degradation of p-nitrophenol and reduction of Cr(VI) in one step using microwave atmospheric pressure plasma. *Water Res.* **2022**, *212*, No. 118124.
(70) Argyle, M. D.; Bartholomew, C. H. Heterogeneous Catalyst Deactivation and Regeneration: A Review. *Catalysts* **2015**, *5*, 145−269.
(71) Bloh, J. Z.; Dillert, R.; Bahnemann, D. W. Transition metal-modified zinc oxides for UV and visible light photocatalysis. *Environ. Sci. Pollut. Res.* **2012**, *19*, 3688−3695.
(72) Bishayee, B.; Ruj, B.; Chakrabortty, S.; Nayak, J. Facile synthesis, characterization and application of heterogeneous Al@Si materials for adsorptive mitigation of fluoride: Optimization and cost analysis. *Environ. Nanotechnol., Monit. Manage.* **2021**, *16*, No. 100490.
(73) Zendehdel, M.; Shoshtari-Yeganeh, B.; Khanmohamadi, H.; Cruciani, G. Removal of fluoride from aqueous solution by adsorption on NaP:HAp nanocomposite using response surface methodology. *Process Saf. Environ. Prot.* **2017**, *109*, 172−191.
(74) Sadhu, K.; Mukherjee, A.; Shukla, S. K.; Adhikari, K.; Dutta, S. Adsorptive removal of phenol from coke-oven wastewater using Gondwana shale, India: experiment, modeling and optimization. *Desalin. Water Treat.* **2014**, *52*, 6492−6504.
(75) Biswas, G.; Pokkatt, P. P.; Ghosh, A.; Kamila, B.; Adhikari, K.; Dutta, S. Valorization of waste micro-algal biomass − collected from coke oven effluent treatment plant and evaluation of sorption potential for fluoride removal. *Water Sci. Technol.* **2018**, *78*, 132−146.
(76) Biswas, G.; Thakurta, S. G.; Chakrabarty, J.; Adhikari, K.; Dutta, S. Evaluation of fluoride bioremediation and production of biomolecules by living cyanobacteria under fluoride stress condition. *Ecotoxicol. Environ. Saf.* **2018**, *148*, 26−36.
(77) Biswas, G.; Kumari, M.; Adhikari, K.; Dutta, S. Application of response surface methodology for optimization of biosorption of fluoride from groundwater using Shorea robusta flower petal. *Appl. Water Sci.* **2017**, *7*, 4673−4690.

https://doi.org/10.1021/acsomega.3c03859
ACS Omega 2023, 8, 42164−42176